Automatic Monitoring of Oil Tank 3D Geometry and Storage Changes With Interferometric Coherence and SAR Intensity Information

Ya-Lun S. Tsai, Chun-Jia Huang, Chia-Ling Chen, and Jen-Yu Han

***Abstract*—Continuous monitoring of oil tanks is vital for analyzing local fuel consumption. Synthetic aperture radar (SAR) has been a popular data source as it guarantees day-and-night and all-weather sensing capacity. However, most earlier studies adopt a scene-wise and oil tank-wise scheme, which is inefficient as there can be hundreds of oil tanks on an oil depot, while only a few are dynamic. Also, no study explores both intensity coherence and interferometric coherence for oil tank dynamics mapping. This article proposes a novel three-stage strategy to detect all oil tanks, identify dynamic oil tanks, and estimate their fuel volume changes based on both the intensity and phase information of SAR in both slant-range and geocoded projections. Results indicate that the intensity coherence can perfectly differentiate dynamic and stable oil tanks (a Jeffries–Matusita distance of 1.997) and is less vulnerable to repeat-pass SAR factors, such as baselines and atmospheric conditions. Via evaluating estimations' consistency, our scattering keypoint detection exhibits 0.23 and 0.87 m precision of tank heights and diameters, respectively. By validation with ground truth data, oil tanks exhibiting floating-roof changes larger than 0.23 m are correctly identified. Also, the estimated storage changes agree well with actual changes with an R-squared value of 0.98 and a root-mean-square error corresponding to 1.05 m biases in floating-roof heights. These quantitative assessments confirm the robustness and broad applicability of our non-in situ data-needed approach, highlighting the opportunity to utilize spotlight SAR data to automatically and comprehensively monitor oil tank dynamics in remote sites.**

***Index Terms*—Object detection, scattering feature extraction, spaceborne remote sensing, synthetic aperture radar (SAR).**

I. Introduction

MONITORING oil tanks has been a vital research topic as regional energy consumption is highly relevant to economic activities [1] and military target reconnaissance [2]. To cost-efficiently monitor large amount of oil tanks at oil depots, spaceborne remote sensing have become a popular data source. Conventional multispectral image-based studies detect oil tanks based on circular shapes and employ techniques, such as Hough transform [3], template matching [4], saliency detection [5], or thresholding segmentation [6]. Nonetheless, as optical images are inevitably affected by clouds and rain, continuous monitoring is unfeasible. Also, the applicability of shadow-based extraction methods, e.g., [3], [6], would be hindered by variant illumination conditions.

In contrast, synthetic aperture radar (SAR), a long-wavelength and active sensing technique, provides all-weather and day-any-night sensing opportunities [7]. However, SAR data have much more complex characteristics than optical data: due to SAR sensors' side-looking echolocation manner, oil tanks would not present regular circular shapes but discrete points with layover effects on images and as SAR sensors coherently record backscattered echoes, oil tanks are difficult to be distinguished from background clutter and speckle. Thus, conventional optical image-targeted approaches are inappropriate for SAR data [2], [8], [9].

Instead, the radar scattering mechanism is the key to correctly extracting of oil tanks on SAR images. As mentioned in [10], by exploiting the SAR scattering mechanism, more details in the vertical structure of oil tanks can be extracted compared to optical sensors. Nonetheless, previous SAR-based oil tank extraction studies demonstrate the following limitations: requiring external data, e.g., optical images [11], [12]; utilizing poor-resolution SAR images (resolution > 2 m) [9], [13]; demanding oil tank geometry information, e.g., radius and height [13] and locations [14]; involving manual selection of backscattering points [15], [16]; relying on nearby land features, e.g., T-shaped harbor [9]; or consuming extensive processing time and computation power [2], [14]. These limitations greatly hinder their methods' universal applicability, especially in regions with many oil tanks, but no ground truth data is available.

On the other hand, because most oil tanks contain volatile oil products with a vapor pressure of less than 11.1 Pisa [17], their roofs are generally designed to float rather than be fixed to reduce the vapor space [18]. Therefore, by exploiting scattering feature points of floating roofs on SAR images, it is feasible to estimate oil tanks' storage changes, as simulated in [15] and demonstrated in [14]. Nonetheless, many recent studies only

Manuscript received 5 September 2023; revised 17 October 2023; accepted 23 November 2023. Date of publication 28 November 2023; date of current version 18 December 2023. *(Corresponding author: Ya-Lun S. Tsai.)*

Ya-Lun S. Tsai is with Earth Observation and Remote Sensing Laboratory, Department of Civil Engineering, National Taiwan University, Taipei 10617, Taiwan (e-mail: yalunstsai@ntu.edu.tw).

Chun-Jia Huang and Jen-Yu Han are with the Center for Research on High-Performance Remote Sensing and Urban Informatics, Department of Civil Engineering, National Taiwan University, Taipei 10617, Taiwan (e-mail: d05521008@ntu.edu.tw; jyhan@ntu.edu.tw).

Chia-Ling Chen is with Surveying and Geospatial Engineering Division, Department of Civil Engineering, National Taiwan University, Taipei 10617, Taiwan (e-mail: chialing1109@gmail.com).

Digital Object Identifier 10.1109/JSTARS.2023.3337126

© 2023 The Authors. This work is licensed under a Creative Commons Attribution-NonCommercial-NoDerivatives 4.0 License. For more information, see https://creativecommons.org/licenses/by-nc-nd/4.0/

extract oil tanks' locations and spatial distributions [9], [11], [19], [20], [21]. Furthermore, to our knowledge, all previous storage change detection studies use scene-wise and oil tank-wise approaches; therefore, they are time-consuming to examine the time series dynamics of all oil tanks located in oil depots. The only literature that explores image-pair analysis is [14]. However, in their sophisticated workflow, the interferometric coherence is only computed at selected pixels (i.e., identified coherent scatterers) to refine the oil tank's geometry estimations. Namely, no study utilizes image pair-derived information for tracking oil tank changes.

Founded on the abovementioned aspects, we recognize that using SAR data for 3-D mapping oil tanks has not been comprehensively explored. To overcome these limitations and further make use of both phase and intensity information stored in SAR data, the main objectives of this article include: exploring both phase-based complex coherence (i.e., interferometric coherence) and intensity-based correlation coherence (i.e., intensity coherence) to detect oil tanks that floating roof have moved (i.e., dynamic oil tanks); utilizing deep learning architecture to automatically delineate all oil tanks' locations; estimating dynamic oil tanks' storage changes via automatically locating scattering keypoints; and establishing a computation-efficient, nonmanual intervention-required, and nonexternal or ground truth data-demanded workflow that maps 3-D oil tank's geometry and dynamics.

The rest of this article is organized as follows: Section II introduces the overall workflow and methodology, Section III demonstrates the tested SAR data and corresponding results, Section IV discusses the significance and limitations of our approach, and Section V concludes the implications of this article.

II. Methodology

A. Overall Workflow

To automatically and efficiently detect all oil tanks in oil depots, identify dynamic oil tanks, and estimate dynamic oil tanks' storage changes, we utilize different SAR-derived information in a three-stage processing strategy. As both phase and intensity are explored, level 1 single-look complex (SLC) images with full native resolution in slant-range geometry are selected. Firstly, to detect all oil tanks on SAR images, the geocoded decibel intensity images are generated and input to the you only look once (YOLO) model [22] for generating each oil tank's bounding box. Then, we examine each bounding box's interferometric and intensity coherence estimated from co-registrated phase and intensity images, respectively, and apply a threshold to identify dynamic oil tanks that floating roofs have moved. Finally, based on each dynamic oil tank's subset slant-range intensity image, its storage changes can be estimated by detecting scattering keypoints and computing 3-D geometry. The overall workflow is illustrated in Fig. 1, with each stage elaborated as follows.

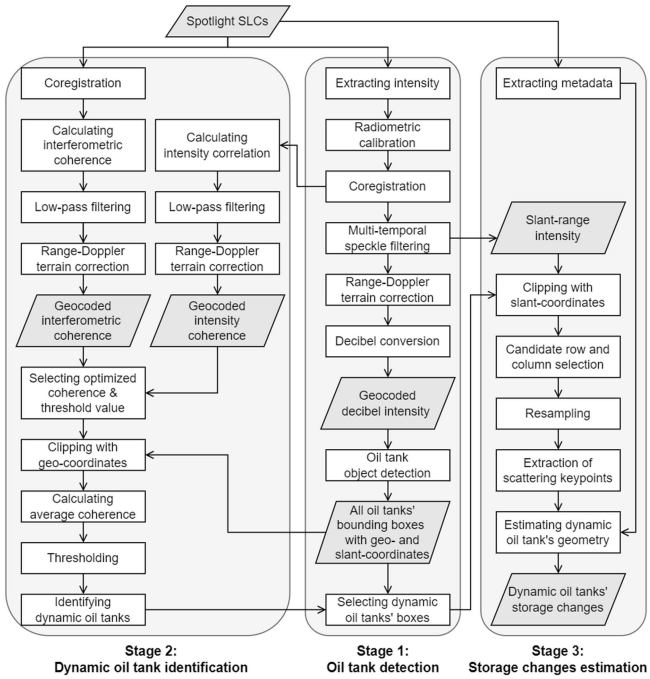

Fig. 1. Overall workflow of the proposed three-stage approach.

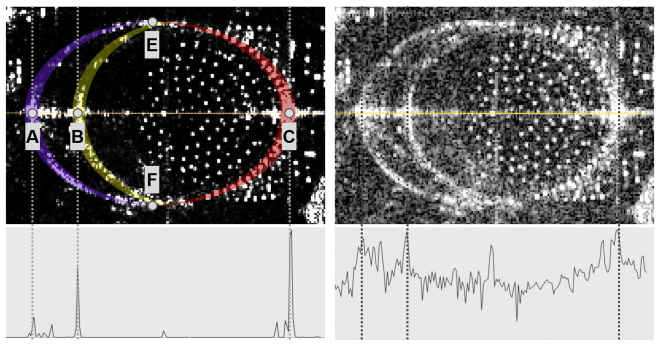

Fig. 2. Scattering features of floating-roof oil tanks on (a) intensity images, (b) intensity images in decibel units. The lower panel histogram represents pixel values along each center row (yellow line). Five geometry-related scattering keypoints are marked in letters A to E.

B. Stage 1: Oil Tank Detection

Since most oil tanks are cylindrical and designed according to conventional standards [23], their geometry and corresponding scattering patterns on SAR images do not significantly vary in different regions or countries. Therefore, an opportunity exists to establish a widely applicable SAR-based oil tank detection method. Specifically, as comprehensively discussed in [14] and [15], most distinct scattering arcs and points result from direct scattering from the top circumferential edge of oil tanks [blue arc in Fig. 2(a)], double reflection between the ground and outer wall of oil tanks [yellow arc in Fig. 2(a)], double reflection between the floating roof and inner wall of oil tanks [red arc in Fig. 2(a)], and double reflection between the floating roof and metal rods on the floating roof [white points between yellow and red arcs in Fig. 2(a)].

While these scattering features are observable in each oil tank, their topology and appearances are sensitive to oil tanks' geometrical details. For instance, a support structure on the roof

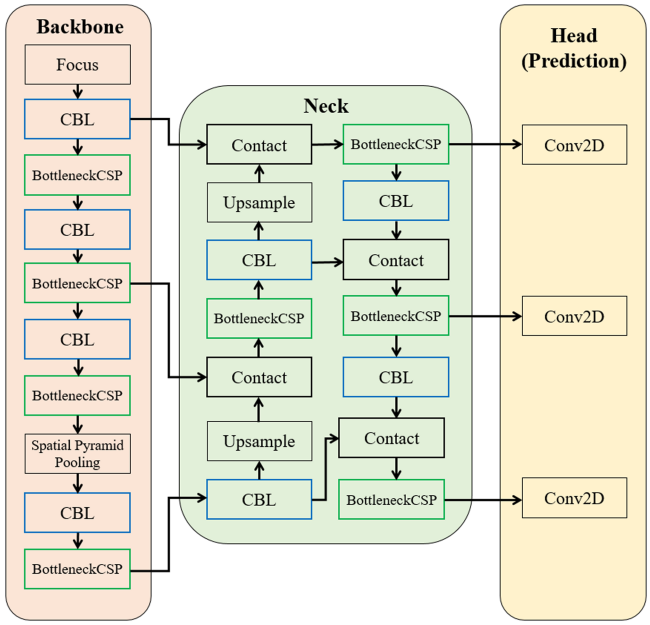

Fig. 3. Schematic illustration of YOLOv5 architecture modified from [30].

or a gangway on the top edge would yield extra scattering arcs [15], and multiple scattering can lead to additional scattering keypoints [2], [13]. Also, the ground materials and corresponding dielectric properties would significantly alter clutter signals, which change the contrast between ground and oil tanks [15]. Due to the abovementioned variant scattering signals, conventional template matching and saliency detection approaches are unfeasible for oil tank detection. Consequently, this article employs a deep learning-based object detection scheme.

Specifically, we employ YOLOv5m, a mature one-stage detector and a region-based object detection network, which is the medium-sized version of YOLO with increased model capacity [22]. The YOLO algorithm improves detection reliability by training with the entire image and thus reduces false positives [24]. In contrast to other detection models, such as single shot multibox detector and RetinaNet, YOLO provides frequent updates, resulting in faster processing and higher accuracy [25]. It has been a popular architecture as it redefines the object detection task as a regression problem, which significantly increases the processing speed [26].

In detail, its architecture comprises three essential components, i.e., the backbone, head, and detection part, as illustrated in Fig. 3. Within the backbone, the input image undergoes a series of transformations through the Focus structure and the convolution, batch normalization and leaky ReLU activation function module (CBL) to extract features. In addition, the initial input image, with a resolution of $640 \times 640 \times 3$, undergoes a slicing operation, resulting in a transformation into a $320 \times 320 \times 12$ feature map. Subsequently, a convolution operation, involving 32 convolution kernels, is applied [27]. YOLOv5 also utilizes the cross-stage-partial connections modules to improve learning ability and computation efficiency compared to YOLOv4 [28]. Also, YOLOv5's neck component incorporates the feature pyramid network and the path aggregation network structure (PAN), enabling layers to convey semantic features while capturing precise positioning features from the bottom to the top. In the head component, there are typically three detection heads, each responsible for detecting objects of different sizes. Thus, feature information of objects at varying scales can be detected [29].

In this article, a training dataset comprising images with visual object classes format labels is employed. Specifically, for objects such as oil tanks in SAR images, the bounding box annotations are slightly larger than the actual size of the tanks, minimizing the inclusion of unnecessary image background to enhance training effectiveness. This approach ensures that the model learns to identify tanks accurately within diverse scenarios. To achieve the best learning and validation, we strategically allocate the data: 70% for model training, 20% for validation to monitor and fine-tune the learning trajectory, and the remaining 10% for external testing to assess real-case performance. This dataset serves as a foundation for model training, allowing the model to learn and accurately identify tanks within the given context.

In detail, the input geocoded intensity images in decibel units are generated by the following steps.

1) Radiometrically calibrating SLCs to sigma nought based on the state vectors.
2) Coregistrating each calibrated intensity image to the reference image at subpixel accuracy.
3) Multitemporally filtering all images' speckle. As time series information is used, a finer spatial resolution can be kept while the same speckle-suppression performance is achieved. The improved Lee sigma filter based on the speckle probability density functions and the minimum-mean-square-error adaptive estimator [31] with a window size of 5×5 is used. This size is chosen because pixels in a 3×3 window are statistically dependent, as discussed in [31], and a larger size inevitably produces an undesired blurring effect on the edges of features.
4) Range-Doppler terrain correction of side-looking geometric distortions. The average ellipsoidal height is used instead of a digital surface model (DSM) as there is no available DSM that includes the height information of oil tanks. Furthermore, to preserve the projection relationship between slant-range and ground-range geometry, each pixel's original slant-range coordinates are documented.
5) Conversion of intensity to decibel units to compress its wide value range.

By ingesting geocoded decibel intensity images to a manually marked label-trained YOLO model, bounding boxes containing each oil tank on the input images can be drawn. Furthermore, since the input images are geocoded, the corner coordinates of each bounding box can be retrieved. To evaluate the correctness, apart from examining the internal accuracy of model training using the mean average precision (mAP) value calculated over multiple intersection of union (IOU) thresholds (from 0.50 to 0.95 with a constant interval of 0.05), the actual detection accuracy is also assessed. Specifically, based on the visual examinations, we compute different evaluation indices, including precision, recall, and F1 score: Precision quantifies the

proportion of correctly predicted target bounding boxes relative to the total predicted bounding boxes; recall indicates the ratio of correctly detected target bounding boxes to the total number of actual target bounding boxes; and F1 score is a composed weighted measurement of precision and recall. Notably, in this article, we only consider bounding boxes that completely contain five scattering keypoints of oil tanks (see Fig. 2) and do not show significant offsets as true positive cases.

C. Stage 2: Dynamic Oil Tank Identification

As mentioned in the introduction, most earlier storage change detection studies use scene-wise and oil tank-wise approaches, which are computation-intensive to examine the time series dynamics of all oil tanks located in oil depots. To improve the efficiency, this article proposes an image pair-based and automatic dynamic oil tank detection approach.

The essence of this approach is exploring both interferometric coherence and intensity coherence, which are computed with phase and intensity, respectively. The former assumes the ground motion-led temporal de-correlation would reduce the interferometric coherence γ_c, which is defined as (1) under the assumption of ergodicity

$$\gamma_c\ (i,j) = \left| \frac{\sum_N c_1\,(i,j)\, c_2^*\,(i,j)}{\sqrt{\sum_N |c_1\,(i,j)|^2 \sum_N |c_2\,(i,j)|^2}} \right| \tag{1}$$

where $c_1(i,j)$ and $c_2(i,j)$ are the complex pixel values of paired SLC images at pixel (i,j), c^* denotes the complex conjugate of c, and N is the number of pixels in the sample window. On the contrary, intensity coherence γ_I only utilizes the intensity value

$$\gamma_I\ (i,j) = \frac{\sum_N I_1\,(i,j)\, I_2^*\,(i,j)}{\sqrt{\sum_N |I_1\,(i,j)|^2 \sum_N |I_2\,(i,j)|^2}} \tag{2}$$

where $I_1(i,j)$ and $I_2(i,j)$ are the pixel values of paired intensity images at pixel (i,j).

Although (1) and (2) are structurally similar, their values are changed with different mechanisms: the interferometric coherence measures the preservation of the phase between paired images, which is not only affected by objects' changes but also SAR sensors' sensing geometry (e.g., spatial baseline) and environment (e.g., atmospheric delay) [32], while the intensity coherence maps the changes in objects' characteristics, e.g., geometry, dielectric properties, and surface roughness [7]. Due to these differences, they are suitable for mapping changes of different magnitudes (the former is more sensitive to subtle deformation, while the latter is suitable for detecting large-scale changes [33], [34]). Despite previous studies have examined their suitability for landslide detection [35] and building damages [34], there is no study explores them for oil tank dynamics tracking.

Practically, in this article, both phase and intensity information of SLCs are extracted and coregistrated. Namely, the calibrated and coregistrated intensity stack described in Section II-B step two is used. Then, both pair-wise coherences are calculated with a window size of 7×7. A larger window than stage one is used because here we do not need to preserve the details of the oil tanks, but rather emphasize the general similarity between paired images to enhance the contrast between stable and dynamic oil tanks. Next, to mitigate the noises in coherences, we apply a median filter with a minimum window size of 3×3 to avoid any additional blurring effect. It should be noted that since here we do not aim to detect the scattering keypoints on oil tanks (i.e., stage one) but calculate the overall areal coherence value of each oil tank, the median filter is used rather than the improved Lee sigma filter aiming at preserving inhomogeneous edges/points. Finally, Range-Doppler terrain correction is performed to yield geocoded interferometric and intensity coherence.

Next, both coherences are compared to select an optimized coherence showing the more significant differentiation between stable and dynamic oil tanks. In addition to visually inspecting the distributions of coherence values, we calculate their Jeffries–Matusita (JM) distance [36] to quantify their inter-class separability, which is defined as

$$J = 2\left(1 - e^{-B}\right) \tag{3}$$

where B is the Bhattacharyya distance between classes (i.e., dynamic and stable oil tanks), which is further rewritten as (4) under the assumption of multivariate normal distribution

$$B = \frac{1}{8}\left(\mu_{\text{dyn}} - \mu_{\text{sta}}\right)^2 \frac{2}{\sigma_{\text{dyn}}^2 + \sigma_{\text{sta}}^2} + \frac{1}{2}\ln\left[\frac{\sigma_{\text{dyn}}^2 + \sigma_{\text{sta}}^2}{2\sigma_{\text{dyn}}\sigma_{\text{sta}}}\right] \tag{4}$$

where μ_{dyn} and μ_{sta} denote the mean and σ_{dyn} and σ_{sta} represent the standard deviation of coherence values of all dynamic and stable oil tank samples. As JM distance is asymptotic to 2.0, a larger JM distance presents a better separability between classes: values less than 1.4 suggest poor separation with significant overlap, values $\in [1.4,\ 1.8)$ suggest moderate separation, values $\in [1.8,\ 1.9)$ indicate fairly good separation, and values $\in [1.9,\ 2.0]$ denote classes fully separated [37].

Based on the chosen coherence (either γ_c or γ_I), an optimized threshold value γ_{thres} is determined based on Otsu's algorithm [38], which is preferred for its simplicity and robustness for binary classifications [7]. Then, together with each oil tank's bounding box extracted in stage one (see Section II-B), we compute the average coherence value of each oil tank γ_{avg}. By applying thresholding with the determined value γ_{thres}, dynamic oil tanks can be identified

$$\begin{cases} \text{Dynamic oil tank} & \text{if } \gamma_{\text{avg}} < \gamma_{\text{thres}} \\ \text{Stable oil tank} & \text{otherwise} \end{cases}. \tag{5}$$

This coherence-based approach enables automatic dynamic oil tank detection, which is particularly valuable when there are hundreds of oil tanks in an oil depot.

D. Stage 3: Storage Changes Estimation

After identifying dynamic oil tanks, we estimate their storage changes which are vital pieces of information for estimating local fuel consumption. To fulfill this aim, the scattering features mentioned in Section II-B and illustrated in Fig. 2 are explored. In detail, because oil tanks are cylindrical, their scattering features are symmetric concerning the range direction. Hence, rather than exploiting the whole scattering arcs, we can

estimate oil tanks' 3-D geometry by only locating the scattering keypoints, i.e., points A, B, C, E, and F marked in Fig. 2(a), which show strong reflections and high intensity values. This simplification has a three-fold advantage: it avoids the difficulty of reconstructing inconsecutive scattering arcs using techniques, such as the Hough transform, which demands heavy calculation and demonstrates false fitting [14]; it avoids the radius bias between the constructed scattering arcs and the actual oil tank shape, as thoroughly discussed in [10]; and it efficiently reduces the number of detected targets and corresponding computation time.

Based on these five points (points A, B, and C locates in the same range direction, while points E and F locates in the same azimuth direction), each oil tank's 3-D geometry (e.g., diameter D, tank height h_{tank}, and floating-roof height h_{float}) can be estimated

$$D = PS_{az}\ (F_{az} - E_{az}) \tag{6}$$

$$h_{\text{tank}} = \frac{PS_{rg}\,(B_{rg} - A_{rg})}{\cos\theta} \tag{7}$$

$$h_{\text{float}} = \frac{PS_{rg}}{\cos\theta}\left[(C_{rg} - B_{rg}) + \frac{D\sin\theta}{PS_{rg}}\right] \tag{8}$$

where F_{az} and E_{az} are azimuth coordinates of points F and E, A_{rg}, B_{rg}, and C_{rg} are range coordinates of points A, B, and C. These coordinates are in pixel units. PS_{az} and PS_{rg} are pixel spacing distance in azimuth and slant-range direction, θ is the incidence angle. Pixel spacing and incidence angle can be extracted from the SLCs product metadata. It should be noted that the pixel spacing may differ from spatial resolution when SLCs are resampled. Eventually, based on these parameters, the stored fuel volume V can be estimated as

$$V = \pi h_{\text{float}}\left(\frac{D}{2}\right)^2. \tag{9}$$

In this article, the coregistrated and filtered intensity stack described in Section II-B step three is used. Namely, we extract scattering keypoints based on slant-range intensity images because: the geocoding processing rotates the alignment of scattering keypoints along the range and azimuth directions, which impedes efficient row- and column-wise searching of scattering keypoints and the decibel conversion reduces the contrast between scattering keypoints and clutter as shown in Fig. 2(b). Noteworthily, stage one (see Section II-B) utilized geocoded decibel intensity images as decibel conversion reduces value range and enables detecting the overall shape of each oil tank, while geocoding processing facilitates retrieving oil tanks' geo-coordinates. In other words, stage one considers each oil tank as an object, while stage three only focuses on each oil tank's scattering keypoints.

Also, since this article aims at tracking dynamic oil tanks' storage changes, only the bounding boxes (extracted in stage one, i.e., Section II-B) of the dynamic oil tanks (identified in stage two, i.e., Section II-C) are utilized to clip the intensity image for the following analysis. The merit of this approach is high efficiency, as based on our experiences, generally there are only a few oil tanks in oil depots that are dynamic, especially when the revisit time of SAR sensors is short. Consequently, rather than extracting all oil tanks' scattering keypoints and estimating their storage changes, performing these steps only on dynamic oil tank detected with coherence is more efficient.

To extract five scattering keypoints, we perform an automatic row- and column-wise peak searching scheme. First, to detect three range direction-aligned and two azimuth direction-aligned keypoints, candidate rows (i.e., the center row of the bounding box plus or minus one-fifth box height) and candidate columns (i.e., the one-third column of the bounding box from the left plus or minus one-fourth box width) are chosen. This selection is because each bounding box is trained to be nearly centered at the oil tank (so three range direction-aligned keypoints should approximately sit at the center row, while the location of two azimuth direction-aligned keypoints vary as floating-roof locations can move).

Next, each candidate's rows and columns are cubically upresampled to a 20-times higher resolution to facilitate subpixel analysis. More importantly, a large upsampling factor converts discrete values between neighboring pixels to a smooth and continuous signal [39], avoiding misconsidering shoulder peaks as actual peaks. Afterward, each row and column is scanned with the multiscale-based peak detection algorithm [40] to detect candidate scattering keypoints (i.e., pixels with peak values). This algorithm is originally developed for electrocardiography, yet due to its robustness in detecting peaks of noisy signals via exploring the local maxima scalogram and does not require users to manually set any hyper-parameter prior to the analysis, it is commonly used in different disciplines [41].

Nevertheless, quality inspection (i.e., checking whether there are more than three and two peaks identified along the range and azimuth directions, respectively) is recommended, as scattering keypoints could be confused with other oil tanks' geometrical details or ground clutters mentioned in Section II-B. Although practically, as found in our study sites, clutter signals from paved surface and multiple scattering would show weaker backscatter coefficients than the double reflections from metal oil tanks, and thus would not be considered as peaks.

Finally, the five actual scattering keypoints are detected from all candidate scattering keypoints by selecting the row and column with the longest pixel distance between keypoints as the actual diameter has the longest profile distance. Eventually, based on five detected scattering keypoints with subpixel resolution, we estimate each dynamic oil tank's 3-D geometry and storage change between each image pair. Thence, a multi-temporal oil tank dynamic tracking and fuel volume assessment can be achieved.

III. Experiments and Results

In this section, we first introduce the datasets and implementation details. Then, each processing stage's results are demonstrated, including accuracy assessment of oil tank detection, selection of the optimized coherence for dynamic oil tank identification, and validations of estimated oil tank geometry and storage changes.

TABLE I
METADATA OF USED TERRASAR-X DATASET

Site	A	B	C
Acquisition mode	HighRes SpotLight 300 MHz (HS300)	HighRes SpotLight 300 MHz (HS300)	HighRes SpotLight 300 MHz (HS300)
Product type	SSC	SSC	SSC
Process level	L1B	L1B	L1B
Polarization	HH	HH	HH
Average incidence angle	50.8°	53.1°	50.6°
Average azimuth pixel spacing (m)	0.861	0.870	0.872
Average slant-range pixel spacing (m)	0.455	0.455	0.455
Acquisition date	January,2,2023	December 28, 2022	January, 2,2023
	January,1,2023	January, 8,2023	January,1,2023
	January, 24,2023	January, 19,2023	January, 24,2023
	February 4, 2023	Januray, 30,2023	February 4, 2023
	February 15, 2023	February 10, 2023	February 15, 2023
	February 26, 2023	February 21, 2023	February 26, 2023
	March 9, 2023	March 15, 2023	March 9, 2023
	March 20,2023	March 26, 2023	March 20, 2023

A. Dataset and Setup

As concluded in previous studies, the discernment of oil tanks' scattering features largely depends on the SAR sensor's resolution. For instance, SAR images with a resolution smaller than or equal to 1 m resolution yield much more reliable height and radius estimations [16], while 3 m resolution images give a lower detection rate [9], [13]. Therefore, we employ *X*-band TerraSAR-X SLC images acquired in the high-resolution spotlight (HS) mode with a bandwidth of 300 MHz, guaranteeing a fine slant-range and azimuth resolution of 0.6 and 1.1 m, respectively. To examine the universal applicability of our proposed workflow, three oil depots (i.e., sites A, B, and C) located in different bay areas are selected. Since there are more than a hundred oil tanks on both sites A and B, the value of our automatic and efficient monitoring scheme is affirmed. Each site's dataset consists of eight TerraSAR-X images, with details given in Table I. Note that the incidence angle and pixel spacing distance would slightly vary between images.

It should be noted that since this article aims at estimating dynamic oil tanks' storage changes, only floating-roof oil tanks at these sites are considered in the following analysis.

In stage one, to train the YOLO model for oil tank detection, we first labeled half of the oil tanks randomly chosen among all eight images of site A (i.e., the A-1 subdataset), where oil tanks' sizes and geometrical details are the most variant. All oil tank samples are carefully outlined during the data labeling procedure. To train the model and examine resultant accuracy, 70%, 20%, and 10% of labeled data are allocated for training, internal validation, and external testing, respectively. Regarding the hyperparameters, we utilize the Adam optimization algorithm with a learning rate of 0.001 and a momentum value of 0.9. The maximum number of training epochs is set as 300. Also, the confidence score threshold is set as 0.5 in the article.

Then, the trained model is used to estimate the bounding boxes of all oil tanks in sites B and C as well as another half of the oil tanks in site A (i.e., the A-2 subdataset). Next, in stage two, all dynamic oil tanks in sites B and C are identified with the optimized coherence and threshold value determined with the A-2 subdataset. Finally, in stage three, the storage changes of all dynamic oil tanks in sites B and C are estimated based on their extracted scattering keypoints. In order to evaluate the precision and accuracy of the estimated oil tank geometry and storage changes, the ground truth data in site C provided by the Chinese Petroleum and Chemical Corporation (CPC) in Taiwan are used for quality evaluations. The overall data splitting and processing stages are illustrated in Fig. 4.

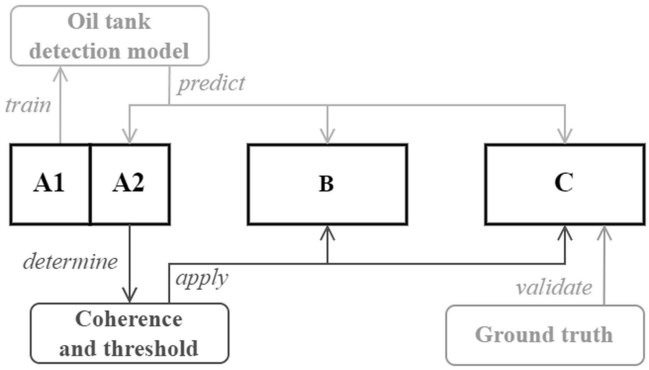

Fig. 4. Overall data splitting and training strategy of three test sites. Different grey colors represent different processing stages.

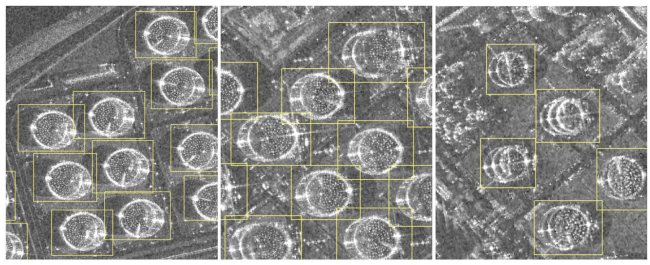

Fig. 5. Visualization of the detected bounding boxes (yellow boxes) for parts of oil tanks of (a) A-2 subdataset, (b) site B, and (c) site C shown over intensity images in decibel units.

B. Accuracy Assessment of Oil Tank Detection

First, we examine the internal accuracy of the model training using the A1 subdataset. A mAP value of 88.1% is found. Considering our methodology during model training, detections with an IOU of 0.5 or higher are incorporated into the precision calculations. Detections below this IOU threshold did not positively contribute to the model's performance metrics. Therefore, a mAP value of 88.1% is deemed acceptable. The trained model demonstrates fairly good performance of oil tank detection, especially considering site A has the most complicatedly shaped and sized oil tanks. Therefore, we apply the trained model on the A-2 subdataset and sites B and C to detect each site's oil tanks.

By visual inspections, it is confirmed that the model can correctly detect all oil tanks in each test site, as exemplified in Fig. 5.

TABLE II
RESULTS OF OIL DETECTION ON DIFFERENT TEST SITES

Site	Precision	Recall	F1
A2	100%	98.2%	99.1%
B	100%	96.2%	98.0%
C	95.6%	94.6%	95.1%

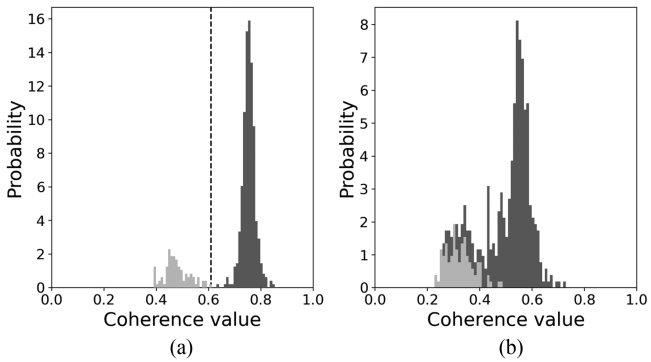

Fig. 6. Distributions of (a) intensity coherence and (b) interferometric coherence values of dynamic (light grey) and stable (dark grey) oil tanks. The determined interclass threshold value is marked with the dotted line.

More importantly, detected bounding boxes match well with oil tanks' centers, guaranteeing the feasibility of stage three's row- and column-wise searching of scattering keypoints. Next, we compute different evaluation indices to assess the practical usability of detected oil tank bounding boxes, as given in Table II. Results indicate our trained YOLO model can generate reasonable bounding boxes for at least 94.6% of oil tanks at three sites, which accuracy satisfy the purpose of this article. In fact, if more SAR images over different sites where oil tanks have variant scattering features due to different geometrical details were used for model training, or employed a more sophisticated detection architecture (e.g., the self-attention component-included transformer network that can learn long-range dependencies between pixels and capture global contextual connections, as used in [13]), the accuracy can be further improved.

C. Selection of Coherence for Dynamic Oil Tank Identification

To select the optimized coherence and threshold value for classifying dynamic and stable oil tanks, the A-2 dataset is used. By visually inspecting each oil tank's floating-roof scattering keypoint (i.e., point C in Fig. 2), among all 516 oil tank samples (each oil tank can be counted more than once, as time series images are used), 92 samples (17.8%) are found dynamic, i.e., oil tanks that floating roof have moved due to either consumption or filling. This disproportion also suggests that previous studies' oil tank-wise screening scheme is inefficient, as only a minority of oil tanks changed.

Then, to compare both intensity and interferometric coherences' stable/dynamic oil tank differentiation capacity, we plot each sample's average coherence value in Fig. 6. First, intensity coherence has an overall higher value (mainly between 0.4 and 0.8) than interferometric coherence (mainly between 0.2 and 0.7). Secondly, for both intensity and interferometric coherence, dynamic and stable oil tanks always present lower and higher values, respectively. Nonetheless, a substantial overlap between them is observed in interferometric coherence. To quantify both coherences' inter-class separability, we calculate their Jeffries–Matusita (JM) distance. Based on all 516 oil tank samples, the JM distance of intensity and interferometric coherence is 1.997 and 1.271, respectively, indicating the former can perfectly distinguish classes, while the latter cannot.

Therefore, because intensity coherence demonstrates a much stronger separability, it is selected as the coherence for identifying dynamic oil tanks. To facilitate automatic classification, an optimized threshold coherence of 0.61 is determined with Otsu's algorithm, which is then applied to all paired images of sites B and C. Because the distribution of coherence demonstrates a bimodal distribution (although a negative skewness is noted), the suitability of the Otsu's algorithm is guaranteed.

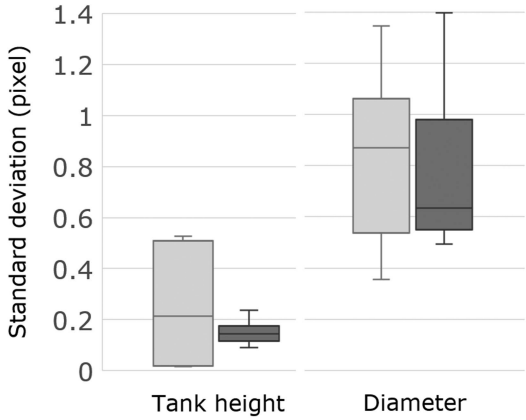

Fig. 7. Internal precisions of the estimated tank heights and diameters of oil tanks on sites B (light grey) and C (dark grey).

D. Evaluations of Estimated Geometry and Storage Changes

Based on the bounding box detected in stage one and the intensity coherence-based identification conducted in stage two, the 3-D geometry and storage changes of all dynamic oil tanks on sites B and C can be estimated via detecting their scattering keypoints.

To evaluate the results' reliability, we first assess the precision of each dynamic oil tank's diameter and tank height. Since both geometries would not vary with time or storage changes, their stability can represent the internal precision of our estimations, i.e., the smaller the standard deviation, the better the precision. Practically, the box plots of the standard deviations of both the estimated diameter and tank height of each oil tank on sites B and C calculated across time/images are plotted in Fig. 7. To enable further uncertainty analysis of the estimated storage changes, standard deviations are presented in pixel units. First, the precision of tank heights is considerably higher than the diameters, as the median standard deviation of the former and latter is approximately 0.2 and 0.8 pixels, respectively. It is because the tank height's scattering keypoints are located along

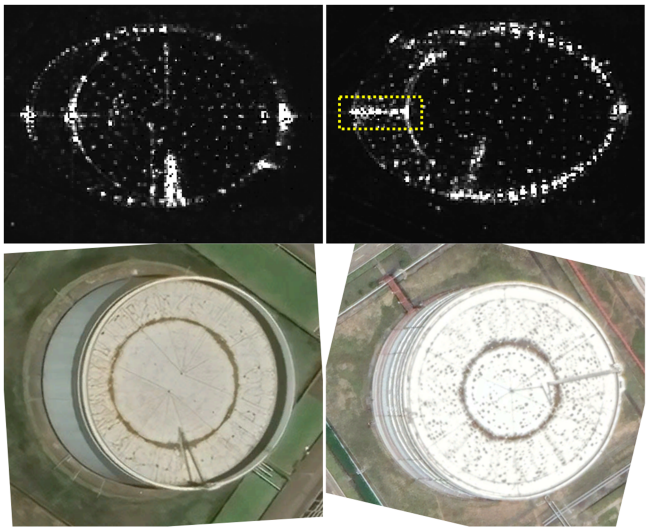

(a) (b)

Fig. 8. Appearance of oil tanks on (a) site B (b) site C in an employed TerraSAR-X spotlight SAR image (upper panel) and an oblique optical image of Google earth (lower panel). Multiple scattering results from support structures on the outer wall of oil tanks are marked with dotted yellow boxes.

the range direction, where strong double reflections happen (as the walls of oil tanks are facing the SAR sensor). Oppositely, the diameter's scattering keypoints stem from the wall of oil tanks nearly orthogonal to the SAR sensing direction, yielding weaker reflections.

Second, site C's tank height estimations are found to be more precise (i.e., a smaller value range) than site B. By inspecting both sites' intensity images, we observe that all of site B's oil tanks exhibit significant multiple scattering, as illustrated in Fig. 8. These additional scattering features likely to result from extra support structures on the outer wall of the oil tank, which are visible on Google Earth's high-resolution optical images.

In conclusion, based on the estimations of both sites B and C, tank height estimations show a higher precision with a third quartile value of a half slant-range pixel, corresponding to 0.23 m. In comparison, the diameter estimations exhibit a relatively lower precision with a third quartile value of nearly one azimuth pixel, i.e., 0.87 m.

In addition to the internal precision examination, we conduct accuracy validation of our estimated storage changes with ground truth provided by CPC. Nonetheless, since CPC only provides the fuel volume records of oil tanks on a subregion of site C, only parts of site C's results can be externally verified. Additionally, because CPC's records are at a 30-min interval, uncertainties in fuel volume caused by temporal gaps are inevitable.

Results indicate that although CPC's data reveal 14 samples showing storage changes, three samples showing the most minor changes among them are not identified dynamic in our stage two coherence-based approach. Based on the CPC's fuel volume records, we inversely calculate these samples' theoretical floating-roof changes [i.e., point C in Fig. 2(a)] in pixels with our

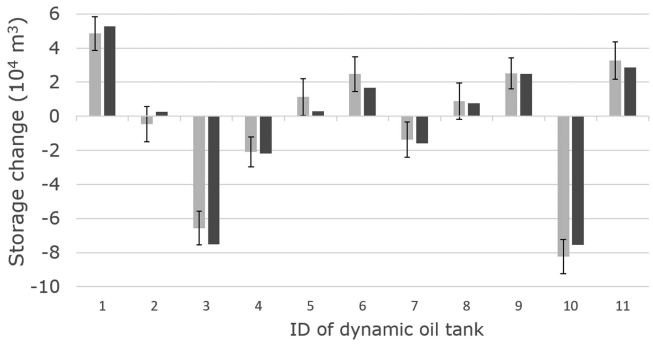

Fig. 9. Estimated (light grey) and ground truth (dark grey) storage changes of dynamic oil tanks on site C.

estimated diameter. The results show that these samples' theoretical slant-range pixel changes are less than half a pixel (0.10, 0.11, and 0.48 pixels, respectively), i.e., 0.23 m. On the contrary, oil tanks showing floating-roof changes larger than 0.23 m are all found to be correctly identified as dynamic samples. We believe it is because the moving window cross-correlation-based coherence approach would inevitably miss these relatively small half-pixel offsets.

Then, by excluding three missed samples, we compare our estimated and the actual storage changes, as plotted in Fig. 9. It should be noted that the expected uncertainties (i.e., the standard deviation) of estimated storage changes are quantified through error propagation analysis of (9) (as discussed in Section II-D, we assume the errors of estimated floating-roof height and diameter is 0.23 and 0.87 m, respectively). Results demonstrate that all eleven samples' actual storage changes are within the uncertainty range of our estimations. This great accuracy can also be confirmed by an R-squared value of 0.98 and a root-mean-square error (RMSE) of around 5808 m^3. This RMSE corresponds to 1.05 m biases in floating-roof height estimations, which is in fact smaller than our expected biases (1.11 m) quantified via error propagation analysis of (8). Namely, the external accuracy agrees with the internal precision. Overall, these evaluations suggest our estimations satisfactorily match well with ground truth data, despite the trend of oil tanks showing storage changes less than propagated uncertainty (e.g., sample two in Fig. 9) may be wrongly depicted.

IV. Discussion

A. Comparison Between Interferometric and Intensity Coherence for Dynamic Oil Tank Identification

The results presented in Section III-C indicate that intensity coherence is more capable of differentiating dynamic and stable oil tanks than interferometric coherence. To the authors' knowledge, it is the first study to examine both coherences' suitability for dynamic oil tank detection. Therefore, exploring the mechanism and other principles behind this finding is necessary.

First, as many earlier studies suggested, intensity coherence is preferred for detecting more significant changes, while interferometric coherence is suitable for mapping trivial or unnoticeable

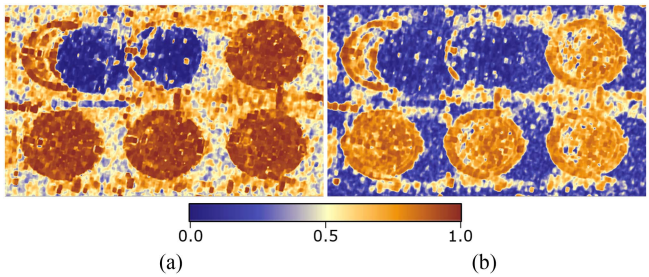

Fig. 10. Appearance of dynamic (top left and top center) and stable oil tanks on (a) intensity coherence and (b) interferometric coherence images.

changes [33], [34]. We deem that the floating roof's dynamic is considerably large when utilizing modern very high-resolution (VHR) spotlight SAR images that have a slant-range resolution near one meter: according to (6), assuming the reliable minimum discernable change of floating-roof scattering keypoints is half a slant-range pixel (based on the precision found in Section III-D) when the incidence angle is less than 60°, the detectable floating height changes is less than one meter, viz., as long as a floating roof moves more than one meter, its changes is reliably visible on a spotlight intensity image and detectable on the corresponding intensity coherence. This theory can be supported by the fact that all oil tanks showing floating-roof changes larger than 0.23 m are corrected identified dynamic, as described in Section III-D. Furthermore, considering most SAR sensors have a revisit time longer than a few days, dynamic oil tanks' roof changes are commonly greater than one meter and, thus, are more suitable to be detected with intensity coherence.

Second, although interferometric coherence is more sensitive to ground objects' changes, it is also vulnerable to different parameters of repeat-pass SAR, such as spatial and temporal baselines. A long temporal baseline implies that ground objects might significantly move or change, and atmospheric conditions might substantially differ [42]. Despite artificial features, such as oil tanks, would not alter their geometry with time, occasional precipitation or dust cover can subtly alter features' dielectric properties and yield random decorrelation [43]. Also, a long spatial baseline beyond the critical baseline can cause paired images' phase to be completely uncorrelated, i.e., an interferometric coherence equals zero [32]. Oppositely, intensity coherence remains much more stable with the same baseline conditions as it is less vulnerable to decorrelation [34], [44]. This mechanism explains stable oil tanks' floating roofs show higher and more concentrated values in intensity coherence (approx. 0.7–0.8) than interferometric coherence (approx. 0.4–0.6), as plotted in Fig. 7 and demonstrated in Fig. 10. In fact, it is the background theory of the Permanent Scatterer SAR interferometry that uses amplitude dispersion to identify stable scatterers for overcoming phase decorrelation [45]. In conclusion, since intensity coherence yields consistent and high values for stable oil tanks, it shows greater contrast between stable/dynamic oil tanks.

Founded on Fig. 10, it is interesting that shadows are much more legible in interferometric coherence. We regard it is because as the shadowed areas' phases are completely random

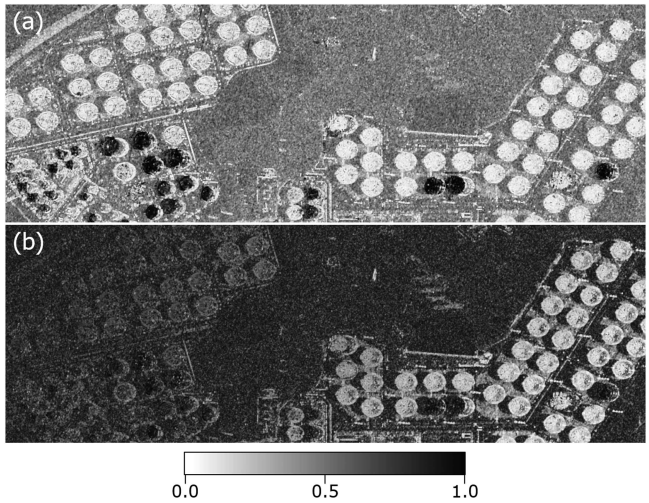

Fig. 11. Overall appearance of (a) intensity coherence and (b) interferometric coherence images.

noises (i.e., noise equivalent sigma zero [46]) in both images (so their interferometric coherence is low) while their intensity values are consistently low. Although this article does not detect oil tanks or estimate geometry based on shadows, this finding may be valuable to some shadow-based studies, e.g., [2].

Finally, intensity coherence is less affected by paired images' atmospheric phase screen (APS) due to the variant atmospheric conditions. By examining each image pair's interferometric coherence, we notice that APS-led effects are commonly found: among all 24 used images, six image pairs show visually clear gradient patterns on interferometric coherence images, as demonstrated in Fig. 11. These patterns are because two paired images' phase signals are modulated with different atmospheric refractivity indices resulting from different temperature, pressure, and humidity (usually exhibit certain spatial patterns), which eventually cause spatially gradient decorrelation [47]. However, notably, this atmospheric effect is trivial in intensity coherence because the intensity is less sensitive to atmospheric refractivity changes unless rain attenuation is evident [48].

B. Limitations and Future Work

In this article, we propose a computation-efficient oil tank 3-D geometry and dynamics mapping strategy by utilizing both the intensity and phase information of SAR images in slant-range and geocoded projections. Although similar to previous studies that are limited by ground truth data availability, only parts of the site C's results are externally validated, revealing that an RMSE corresponds to 1.05 m biases in floating roof heights; we also examine the internal precision of estimations, indicating the error of floating-roof height and diameter of the roof is 0.23 and 0.87 m, respectively. We anticipate this approach can be applied to other oil depots apart from three test sites to facilitate the comprehensive and automatic monitoring of many oil tanks. Nevertheless, there is future potential to improve the current approach and results.

First, whilst intensity coherence has more flexible requirements for paired images' baselines, it still demands both images

acquired with the same viewing geometry (e.g., ascending or descending) and path number (or relative orbit). Otherwise, significantly different geometric distortions, i.e., foreshortening and layover, would hinder the correct coregistration of images. In fact, this requirement can be exemplified by the failure of our preliminary testing using the latest UMBRA, ICEYE and Capella microsatellite images due to the incapability of coregistration and coherence estimation so far. Nonetheless, as demonstrated in [49], the scattering keypoints of oil tanks can still be correctly identified. Namely, once these CubeSats reach satisfactory orbital configurations, the workflow proposed in this article can be efficiently applied. More importantly, as revealed in Section III-D, trivial floating root movements less than 0.23 m cannot be identified using our proposed coherence-based approach. Thus, once these ultrafine submeter resolution microsatellite images are coregistratable, these dynamic oil tanks' storage changes can also be retrieved.

In addition, SAR sensors' look and azimuth angles are vital to ensure the correct extraction of scattering keypoints. Since our proposed strategy exploits the contrast between strong keypoints caused by double reflections and relatively weaker clutter/multiple-scattering signals, the occurrence of the double reflection scattering mechanism is essential to guarantee the successful keypoint extraction. Nonetheless, as simulated in [15], when oil tanks in the vicinity are perfectly aligned in the SAR sensors' range direction, the near-range tank's shadow could hinder the double reflection resulted from the far-range tank's outer wall and the ground in front of it [i.e., the yellow arc in Fig. 2(a)]. In fact, shadowed areas will increase with a larger look angle of sensors. Consequently, point B on Fig. 2 cannot be identified, and thus both tank height and floating-roof height cannot be determined. In this extreme scenario, the whole scattering arc needs to be reconstructed. However, rather than the computationally intensive Hough transform used in an earlier study [14], we consider that efficient edge detection algorithms, such as the active contour model [50], should be explored.

Finally, apart from floating-roof oil tanks analyzed in the current study, fixed-roof oil tanks should be included in the proposed workflow with a more sophisticated strategy. To the authors' knowledge, there is only one study that addresses the 3-D geometry of fixed-roof oil tanks [14]; yet, no study has detected their storage changes. It is because fixed-roof oil tanks would not demonstrate detectable shape changes when fuel volume changes. In other words, the pixel-wise coherence-based method proposed in this article is inapplicable. Instead, we consider the interferometric SAR technique should be employed as it is capable of detecting subtle changes in objects via exploiting paired images' relative phase difference (i.e., fractions of a wavelength) [51], [52]. Thus, the slight expansion (i.e., millimeters to centimeters) of the outer wall of fixed-roof oil tanks may be detected, facilitating the inverse estimations of storage changes.

V. Conclusion

This article proposes an automatic and nonexternal data-required approach that can depict oil tanks' 3-D geometry and storage changes. Both phase and intensity of SAR data in both slant-range and geocoded projections are utilized in a three-stage workflow. First, all oil tanks are detected with the YOLO architecture. Then, we investigate the suitability of two coherences for identifying dynamic oil tanks. Finally, dynamic oil tanks' 3-D geometry and fuel volume are estimated with scattering keypoints extracted with the proposed peak searching scheme. The essence of our approach overcomes the limitations of previous studies that utilize scene-wise and oil tank-wise manner, which is time-consuming and inefficient to scan all oil tanks in oil depots as generally only a few oil tanks are dynamic. Moreover, to the authors' knowledge, it is the first study that uses an image-pair analysis scheme and explores both intensity- and phase-based coherence for dynamic oil tank detection.

By employing spotlight SLC images of three test sites, we can thoroughly inspect the robustness of results and further discuss the mechanism and strengths. First, intensity coherence can ideally differentiate dynamic and stable oil tanks (JM distance of 1.997), while interferometric coherence cannot (JM distance of 1.271). It is because floating roofs' changes are considerably large when utilizing VHR spotlight SAR images and thus, interferometric coherence suitable for detecting trivial changes is not applicable. Moreover, intensity coherence is less vulnerable to repeat-pass SAR variations, such as long baselines and atmospheric conditions. Second, by assessing dynamic oil tanks' estimated diameters and tank heights, a relatively higher precision of tank heights (half a slant-range pixel, i.e., 0.23 m) than diameters (one azimuth pixel, i.e., 0.87 m) is found. It is because height-related scattering keypoints align in the range direction, where strong double reflections happen. Nevertheless, a decrease in height estimations' precision results from multiple scatterings of additional support structures on the oil tank outer walls is also observed on one test site. Finally, by validation with ground truth records of fuel volume, it is revealed that oil tanks exhibiting floating-roof changes more significant than half a slant-range pixel (i.e., 0.23 m) can be correctly identified as dynamic. Also, the actual storage changes are within the uncertainty range of our estimations and demonstrate a perfect R-squared value of 0.98. By conducting uncertainty analysis via error propagation, the observed errors are also found to be smaller than the expected errors. These quantitative evaluations confirm the reliability and accuracy of our approach.

Furthermore, because our approach does not require external data (e.g., optical images) or ground truth information (e.g., locations and geometry), its broad applicability is expected. It can be exemplified by the satisfactorily consistent results of three test sites. In addition, since no manual intervention is needed, this approach enables automatic and efficient monitoring of hundreds of oil tanks' storage changes and 3-D geometry on sites. These pieces of information are valuable for investigating local fuel consumption and filling. In conclusion, this article provides an efficient and feasible oil tank monitoring strategy founded on the modern spotlight SAR data, which is expected to be valuable for the increasing number of microsatellite SAR sensors.

ACKNOWLEDGMENT

The authors would like to thank the Chinese Petroleum and Chemical Corporation in Taiwan for providing the ground truth data used in our study.

REFERENCES

[1] M. Semadeni, "Storage of energy, overview," *Encyclopedia Energy*, vol. 5, pp. 719–738, 2004.
[2] H. Xu, W. Chen, B. Sun, Y. Chen, and C. Li, "Oil tank detection in synthetic aperture radar images based on quasi-circular shadow and highlighting arcs," *J. Appl. Remote Sens.*, vol. 8, no. 1, pp. 083689–083689, 2014.
[3] A. O. Ok and E. Başeski, "Circular oil tank detection from panchromatic satellite images: A new automated approach," *IEEE Geosci. Remote Sens. Lett.*, vol. 12, no. 6, pp. 1347–1351, Jun. 2015.
[4] A. Tadros, S. Drouyer, and R. G. von Gioi, "A contrario oil tank detection with patch match completion," in *Proc. IEEE Int. Geosci. Remote Sens. Symp.*, 2021, pp. 4900–4903.
[5] M. Jing, D. Zhao, M. Zhou, Y. Gao, Z. Jiang, and Z. Shi, "Unsupervised oil tank detection by shape-guide saliency model," *IEEE Geosci. Remote Sens. Lett.*, vol. 16, no. 3, pp. 477–481, Mar. 2019.
[6] T. Wang, Y. Li, S. Yu, and Y. Liu, "Estimating the volume of oil tanks based on high-resolution remote sensing images," *Remote Sens.*, vol. 11, no. 7, 2019, Art. no. 793.
[7] Y.-L. S. Tsai, I. Klein, A. Dietz, and N. Oppelt, "Monitoring large-scale inland water dynamics by fusing sentinel-1 SAR and Sentinel-3 altimetry data and by analyzing causal effects of snowmelt," *Remote Sens.*, vol. 12, no. 23, 2020, Art. no. 3896.
[8] C. Ma et al., "End-to-end method with transformer for 3-D detection of oil tank from single SAR image," *IEEE Trans. Geosci. Remote Sens.*, vol. 60, Nov. 2022, Art. no. 5217619.
[9] L. Chun, X. Chunhua, Y. Jian, X. Yingying, and B. Junliang, "A method for coastal oil tank detection in polarimetrie SAR images based on recognition of T-shaped harbor," *J. Syst. Eng. Electron.*, vol. 29, no. 3, pp. 499–509, 2018.
[10] Y. Zhang, C. Ding, X. Qiu, and F. Li, "The characteristics of the multipath scattering and the application for geometry extraction in high-resolution SAR images," *IEEE Trans. Geosci. Remote Sens.*, vol. 53, no. 8, pp. 4687–4699, Aug. 2015.
[11] R. Zhang et al., "Optical-enhanced oil tank detection in high-resolution SAR images," *IEEE Trans. Geosci. Remote Sens.*, vol. 60, Oct. 2022, Art. no. 5237112.
[12] Y. Wang, M. Tang, T. Tan, and X. Tai, "Detection of circular oil tanks based on the fusion of SAR and optical images," in *Proc. 3rd Int. Conf. Image Graph.*, 2004, pp. 524–527.
[13] C. Ma et al., "Structural projection points estimation and context priors for oil tank storage estimation in SAR image," *ISPRS J. Photogramm. Remote Sens.*, vol. 194, pp. 267–285, 2022.
[14] C. V. Lopez and U. Stilla, "Monitoring of oil tank filling with spaceborne SAR using coherent scatterers," *IEEE J. Sel. Topics Appl. Earth Observ. Remote Sens.*, vol. 14, pp. 5638–5655, May 2021.
[15] H. Hammer, S. Kuny, and K. Schulz, "Simulation-based signature analysis of fuel storage tanks in high-resolution SAR images," *IEEE Geosci. Remote Sens. Lett.*, vol. 14, no. 8, pp. 1278–1282, Aug. 2017.
[16] R. Guida, A. Iodice, and D. Riccio, "Assessment of TerraSAR-X products with a new feature extraction application: Monitoring of cylindrical tanks," *IEEE Trans. Geosci. Remote Sens.*, vol. 48, no. 2, pp. 930–938, Feb. 2010.
[17] S. Pullarcot, *Above Ground Storage Tanks: Practical Guide to Construction, Inspection, and Testing*. Boca Raton, FL, USA: CRC Press, 2015.
[18] D. Wu and Z. Chen, "Quantitative risk assessment of fire accidents of large-scale oil tanks triggered by lightning," *Eng. Failure Anal.*, vol. 63, pp. 172–181, 2016.
[19] L. Zhang and C. Liu, "Oil tank extraction based on joint-spatial saliency analysis for multiple SAR images," *IEEE Geosci. Remote Sens. Lett.*, vol. 17, no. 6, pp. 998–1002, Jun. 2020.
[20] Q. Wu, B. Zhang, C. Xu, H. Zhang, and C. Wang, "Dense oil tank detection and classification via YOLOX-TR network in large-scale SAR images," *Remote Sens.*, vol. 14, no. 14, 2022, Art. no. 3246.
[21] L. Zhang, S. Wang, C. Liu, and Y. Wang, "Saliency-driven oil tank detection based on multidimensional feature vector clustering for SAR images," *IEEE Geosci. Remote Sens. Lett.*, vol. 16, no. 4, pp. 653–657, Apr. 2019.
[22] P. Jiang, D. Ergu, F. Liu, Y. Cai, and B. Ma, "A review of YOLO algorithm developments," *Procedia Comput. Sci.*, vol. 199, pp. 1066–1073, 2022.
[23] A. P. Institute, *API Standard 650: Welded Steel Tanks for Oil Storage*. Washington, DC, USA: Amer. Petroleum Inst., 1998.
[24] N. M. Krishna, R. Y. Reddy, M. S. C. Reddy, K. P. Madhav, and G. Sudham, "Object detection and tracking using YOLO," in *Proc. 3rd Int. Conf. Inventive Res. Comput. Appl.*, 2021, pp. 1–7.
[25] L. Tan, T. Huangfu, L. Wu, and W. Chen, "Comparison of RetinaNet, SSD, and YOLO v3 for real-time pill identification," *BMC Med. Inform. Decis. Mak.*, vol. 21, pp. 1–11, 2021.
[26] M. U. Sumagayan et al., "You only look once on power line components: An object detection using unmanned aerial vehicle," in *Proc. IEEE 13th Int. Conf. Humanoid, Nanotechnol., Inf. Technol., Commun. Control, Environ., Manage.*, 2021, pp. 1–6.
[27] F. Zhou, H. Zhao, and Z. Nie, "Safety helmet detection based on YOLOv5," in *Proc. IEEE Int. Conf. Power Electron., Comput. Appl.*, 2021, pp. 6–11.
[28] T. Jintasuttisak, E. Edirisinghe, and A. Elbattay, "Deep neural network based date palm tree detection in drone imagery," *Comput. Electron. Agriculture*, vol. 192, 2022, Art. no. 106560.
[29] M. Karthi, V. Muthulakshmi, R. Priscilla, P. Praveen, and K. Vanisri, "Evolution of YOLO-v5 algorithm for object detection: Automated detection of library books and performace validation of dataset," in *Proc. Int. Conf. Innov. Comput., Intell. Commun. Smart Elect. Syst.*, 2021, pp. 1–6.
[30] J. Ieamsaard, S. N. Charoensook, and S. Yammen, "Deep learning-based face mask detection using YOLOv5," in *Proc. 9th Int. Elect. Eng. Congr.*, 2021, pp. 428–431.
[31] J.-S. Lee, J.-H. Wen, T. L. Ainsworth, K.-S. Chen, and A. J. Chen, "Improved sigma filter for speckle filtering of SAR imagery," *IEEE Trans. Geosci. Remote Sens.*, vol. 47, no. 1, pp. 202–213, Jan. 2009.
[32] H. A. Zebker and J. Villasenor, "Decorrelation in interferometric radar echoes," *IEEE Trans. Geosci. Remote Sens.*, vol. 30, no. 5, pp. 950–959, Sep. 1992.
[33] M. Preiss, D. A. Gray, and N. J. S. Stacy, "Detecting scene changes using synthetic aperture radar interferometry," *IEEE Trans. Geosci. Remote Sens.*, vol. 44, no. 8, pp. 2041–2054, Aug. 2006.
[34] S. Plank, "Rapid damage assessment by means of multi-temporal SAR—A comprehensive review and outlook to Sentinel-1," *Remote Sens.*, vol. 6, no. 6, pp. 4870–4906, 2014.
[35] J. Jung and S.-H. Yun, "Evaluation of coherent and incoherent landslide detection methods based on synthetic aperture radar for rapid response: A case study for the 2018 Hokkaido landslides," *Remote Sens.*, vol. 12, no. 2, 2020, Art. no. 265.
[36] P. H. Swain and S. M. Davis, "Remote sensing: The quantitative approach," *IEEE Trans. Pattern Anal. Mach. Intell.*, vol. 3, no. 6, pp. 713–714, Nov. 1981.
[37] C. S. Silva and A. R. Marcal, "Colour-based dermoscopy classification of cutaneous lesions: An alternative approach," *Comput. Methods Biomech. Biomed. Eng., Imag. Vis.*, vol. 1, no. 4, pp. 211–224, 2013.
[38] N. Otsu, "A threshold selection method from gray-level histograms," *IEEE Trans. Syst., Man, Cybern.*, vol. 9, no. 1, pp. 62–66, Jan. 1979.
[39] M. Z. Hussain, M. Irshad, M. Sarfraz, and N. Zafar, "Interpolation of discrete time signals using cubic spline function," in *Proc. 19th Int. Conf. Inf. Vis.*, 2015, pp. 454–459.
[40] F. Scholkmann, J. Boss, and M. Wolf, "An efficient algorithm for automatic peak detection in noisy periodic and quasi-periodic signals," *Algorithms*, vol. 5, no. 4, pp. 588–603, 2012.
[41] T. C. Huang and Y. M. Wu, "A robust algorithm for automatic p-wave arrival-time picking based on the local extrema scalogram," *Bull. Seismol. Soc. Amer.*, vol. 109, no. 1, pp. 413–423, 2019.
[42] Y.-L. S. Tsai, A. Dietz, N. Oppelt, and C. Kuenzer, "Wet and dry snow detection using sentinel-1 SAR data for mountainous areas with a machine learning technique," *Remote Sens.*, vol. 11, no. 8, 2019, Art. no. 895.
[43] J. Jung, D.-J. Kim, M. Lavalle, and S.-H. Yun, "Coherent change detection using InSAR temporal decorrelation model: A case study for volcanic ash detection," *IEEE Trans. Geosci. Remote Sens.*, vol. 54, no. 10, pp. 5765–5775, Oct. 2016.
[44] B. Chen, K. Deng, H. Fan, and Y. Yu, "Combining SAR interferometric phase and intensity information for monitoring of large gradient deformation in coal mining area," *Eur. J. Remote Sens.*, vol. 48, no. 1, pp. 701–717, 2015.
[45] A. Ferretti, C. Prati, and F. Rocca, "Permanent scatterers in SAR interferometry," *IEEE Trans. Geosci. Remote Sens.*, vol. 39, no. 1, pp. 8–20, Jan. 2001.

[46] M. Boldt, A. Thiele, K. Schulz, and S. Hinz, "Structural analysis of forest areas in high-resolution SAR images," 2011.
[47] J.-R. Kim et al., "Investigation of potential volcanic risk from Mt. Baekdu by DInSAR time series analysis and atmospheric correction," *Remote Sens.*, vol. 9, no. 2, 2017, Art. no. 138.
[48] F. Marzano et al., "Potential of high-resolution detection and retrieval of precipitation fields from X-band spaceborne synthetic aperture radar over land," *Hydrol. Earth Syst. Sci.*, vol. 15, no. 3, pp. 859–875, 2011.
[49] D. Muff et al., "The ICEYE constellation-some new achievements," in *Proc. IEEE Radar Conf.*, 2022, pp. 1–4.
[50] Y.-L. S. Tsai, "Monitoring 23-year of shoreline changes of the Zengwun Estuary in Southern Taiwan using time-series Landsat data and edge detection techniques," *Sci. Total Environ.*, vol. 839, 2022, Art. no. 156310.
[51] P. A. Rosen et al., "Synthetic aperture radar interferometry," *Proc. IEEE*, vol. 88, no. 3, pp. 333–382, Mar. 2000.
[52] Y.-L. S. Tsai, S.-Y. Lin, J.-R. Kim, and Y. Choi, "Analysis of the seasonal velocity difference of the Greenland Russell glacier using multisensor data," *Terr., Atmospheric Ocean. Sci.*, vol. 30, no. 4, pp. 541–562, 2019.